



## Research Paper

Effects of  $\text{CoAl}_2\text{O}_4$  inoculants on microstructure and mechanical properties of IN718 processed by selective laser meltingI-Ting Ho<sup>a,b</sup>, Tzu-Hou Hsu<sup>a</sup>, Yao-Jen Chang<sup>a</sup>, Chen-Wei Li<sup>c</sup>, Kai-Chun Chang<sup>a</sup>, Sammy Tin<sup>b,\*</sup>, Koji Kakehi<sup>c</sup>, An-Chou Yeh<sup>a,\*</sup><sup>a</sup> Department of Materials Science and Engineering, National Tsing Hua University, Hsinchu, Taiwan ROC<sup>b</sup> Department of Mechanical, Materials and Aerospace Engineering, Illinois Institute of Technology, Chicago, IL, USA<sup>c</sup> Department of Mechanical Engineering, Tokyo Metropolitan University, Tokyo, Japan

## ARTICLE INFO

## Keywords:

Selective laser melting

Superalloys

Inoculant

Tensile properties

Creep properties

## ABSTRACT

This work investigated the effects of  $\text{CoAl}_2\text{O}_4$  inoculants on the microstructure and mechanical properties of a superalloy – Inconel 718 (IN718), processed by selective laser melting (SLM). IN718 powder was blended with 0.2 wt. % of  $\text{CoAl}_2\text{O}_4$  particles. After the SLM process, the  $\text{CoAl}_2\text{O}_4$  particles reacted with IN718 and formed a dispersion of Al-rich nano-oxide particles in the matrix. These inoculants were observed to facilitate the formation of fine, equiaxed grains and reduce the degree of crystallographic texture in the as-built microstructure. The presence of the nano-oxide particles in the microstructure served to restrict the mobility of grain boundaries during heat-treatment and promoted the formation of a bimodal grain structure with comparatively finer average size. Due to the reduction of crystallographic texture, the elastic anisotropy present in as-built specimens was greatly minimized with the addition of  $\text{CoAl}_2\text{O}_4$  inoculants. Specimens containing inoculants were also found to possess improved tensile properties following heat-treatment at both room temperature and 650 °C. Furthermore, creep testing at 650 °C/650 MPa revealed that the steady strain rate of IN718 was lowered from  $8.8 \times 10^{-9} \text{ s}^{-1}$  to  $4.9 \times 10^{-9} \text{ s}^{-1}$ , and the creep rupture life was extended by 52 hours in samples that were fabricated with  $\text{CoAl}_2\text{O}_4$ . These results strongly suggest that the decomposition of  $\text{CoAl}_2\text{O}_4$  into Al-rich oxides during SLM processing not only contributes to grain refinement and a reduction in the degree of crystallographic texture but also forms an oxide dispersion that restricts the mobility of dislocations and grain boundaries in IN718.

## 1. Introduction

Inconel 718 (IN718) is one of the most widely-used superalloys due to a good balance of physical and mechanical properties. Numerous studies have been conducted to investigate the properties of IN718 processed by selective laser melting (SLM) [1–12]. The characteristically high thermal gradient and rapid cooling rate incurred during SLM processing tend to promote the formation of columnar grain structures with strong anisotropy along the [001] or [101] direction which can lead to hot tearing during fabrication. The crystallographic anisotropy present in the as-built microstructure may persist even following a standard post-heat-treatment and affect mechanical properties.

To improve the anisotropic grain structure in metals built by SLM, minor amount of particles with high melting point have been added as inoculants into alloy powders before fusion. Inoculant particles were

reported to facilitate the formation of equiaxed grains and augment the tensile properties of Al7075 alloy [13]. Other investigations were conducted to elucidate the effects of inoculants on the microstructure and mechanical properties of stainless steels and titanium alloys [14–16]. In some cases, the decomposition of inoculants could form stable or metastable phases that served as heterogeneous nucleation sites for grains [17]. In SLM processed austenitic stainless steels with additions of carbides, the tensile strength was found to increase significantly owing to refined grain structure combined with a dispersion of nano-scale  $\text{VC}_x$  particles [17]; similar findings were reported in additively manufactured Al-12Si alloy with  $\text{TiB}_2$  microparticles whose compressive strength was increased significantly [18]. There are some studies focusing on the mechanical properties of IN718 based metal matrix composites (MMCs) fabricated by SLM process, including graphene/IN718 [19], TiC/IN718 [20], WC/IN718 [21], etc., however, to the best of authors' knowledge, the role of these ceramic constituents as

\* Corresponding authors.

E-mail addresses: [tin@iit.edu](mailto:tin@iit.edu) (S. Tin), [yehac@mx.nthu.edu.tw](mailto:yehac@mx.nthu.edu.tw) (A.-C. Yeh).<https://doi.org/10.1016/j.addma.2020.101328>

Received 10 December 2019; Received in revised form 4 May 2020; Accepted 9 May 2020

Available online 25 May 2020

2214-8604/ © 2020 Elsevier B.V. All rights reserved.

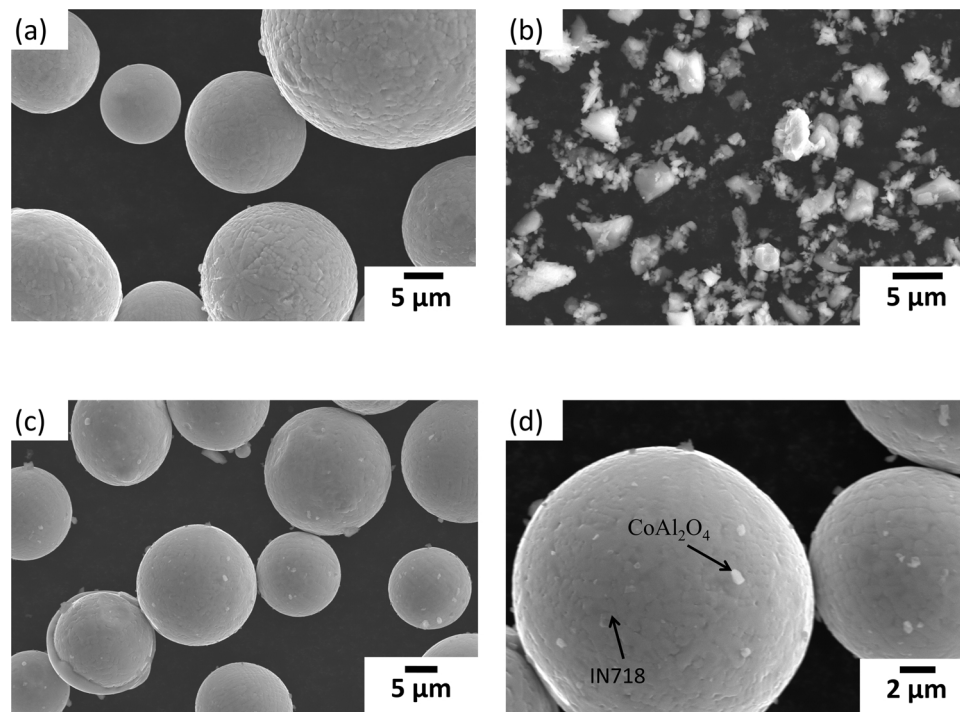


Fig. 1. SEM images showing the powders of IN718 (a) and  $\text{CoAl}_2\text{O}_4$  (b) used for SLM. The morphology of mixed powders of IN718 with 0.2 wt. % of  $\text{CoAl}_2\text{O}_4$  particles are shown in (c) and (d).

inoculants in superalloys is still unclear.

For investment cast superalloys,  $\text{CoAl}_2\text{O}_4$  particles have been widely utilized as inoculants to promote the formation of fine equiaxed grains [22–24]. During solidification, the chemical reaction between  $\text{CoAl}_2\text{O}_4$  particles and elemental Cr, Ti, and Al in the liquid alloy leads to the formation of elemental Co or CoAl intermetallic. Since Co and CoAl both possess a higher melting temperature than IN718, solid particles should survive in the melt and aid in the nucleation of equiaxed grains.

In this investigation, a mixture consisting of 99.8 wt. % of IN718 and 0.2 wt. % of  $\text{CoAl}_2\text{O}_4$  particles were blended and used to fabricate specimens by SLM. Specimens without inoculant were also produced and used to benchmark and quantify the influence of the  $\text{CoAl}_2\text{O}_4$  inoculant particles.

## 2. Material and methods

The IN718 powder used in this study was gas atomized powder (supplied by Chia Yi Steel Inc.) with  $D_{10}=19\ \mu\text{m}$ ,  $D_{50}=32\ \mu\text{m}$ , and  $D_{90}=55\ \mu\text{m}$  (see Fig. 1 (a)); the composition was characterized by ICP Atomic Emission Spectroscopy and carbon/sulfur analyzer which is given in Table 1. Fig. 1 (b) shows the irregular morphology of  $\text{CoAl}_2\text{O}_4$  particles (supplied by Alfa Aesar Inc.) with  $D_{10}=0.3\ \mu\text{m}$ ,  $D_{50}=2.6\ \mu\text{m}$ , and  $D_{90}=6.1\ \mu\text{m}$ . 0.2 wt. % of  $\text{CoAl}_2\text{O}_4$  powder was blended with IN718 powder using a roller mill with a speed of 130 rpm for 1 h. As shown in Fig. 1 (c) and 1 (d),  $\text{CoAl}_2\text{O}_4$  particles were embedded onto the surface of IN718 particles after the blending procedure.

An in-house SLM machine at the National Tsing Hua University was used; selective laser melting was conducted under Ar atmosphere with

**Table 1**  
Nominal composition of IN718 powder used for SLM in wt. % and at. %, respectively.

	Ni	Co	Cr	Fe	Al	Cu	Ti	Si	Mn	Mo	Nb	C
wt. %	Bal.	0.1	18.3	16.8	0.6	0.04	1	0.1	0.1	3	5.2	0.06
at. %	Bal.	0.1	20.4	17.4	1.2	0.04	1.2	0.3	0.1	1.8	3.2	0.3

an oxygen level below 2000 ppm. Following each scan, the powder bed was replenished with a 50  $\mu\text{m}$  layer thickness using a rubber recoater. A YLR-AC-500W Ytterbium fiber laser with a beam size of 58  $\mu\text{m}$  was utilized to produce specimens. Optimized scanning parameters including a laser power of 220 W, a hatch distance of 100  $\mu\text{m}$ , a scanning speed of 800 mm/s, and a zig-zag scanning strategy with an angle of 67° rotation between successive layers were applied; rectangular bars with the dimensions of 80 mm x 15 mm x 10 mm were fabricated on a carbon steel base-plate. After the SLM process, samples were detached from the base-plate by electrical discharge machining; the detached samples were then polished and inspected by the optical microscope. Through the analysis of fraction of porosity using ImageJ software, all specimens fabricated by optimized scanning parameters were found to possess a final density over 99.5 %.

The post-heat-treatment used in this study was a full solution heat-treatment (SHT) and age. Unlike conventional cast and wrought IN718 that requires  $\delta$  phase to stabilize the grain boundaries [25,26], the presence of  $\delta$  phase would inhibit the elimination of texture in parts fabricated by SLM. Thus, the standard SHT condition was not employed in this study; instead, the SHT was conducted at 1100 °C, which is above the solvus temperature of  $\delta$  phase, for 2 hours, followed by air-cooling to ambient temperature [26,27]. After the SHT, specimens were further aged at 720 °C for 8 hours, followed by 620 °C for 8 hours before air-cooling. The aging conditions were based on the standard heat-treatment for cast and wrought IN718 [28].

Specimens for microstructural characterization were prepared using standard metallographic procedures and etched using a Kalling's No. 2 solution (5 g of  $\text{CuCl}_2$  + 100 ml of HCL + 100 ml of ethanol). Microstructures were observed under the scanning electron microscope (SEM, JEOL JSM-7610 F), equipped with an Oxford Instruments INCA energy dispersive X-ray spectroscopy (EDS) detector and Channel 5-HKL electron back-scattered diffraction (EBSD) system. EBSD was conducted under 15 kV; subsequent analysis including grain size distribution and misorientation were performed by EBSD Channel 5-HKL software and Matlab (MTEX toolbox was used), in which over 250 grains were included. Observations under higher magnification were

conducted with the transmission electron microscope (TEM, JEOL JEM-F200) operating at 200 kV. Specimens for TEM analysis were first ground with SiC grinding paper to a thickness below 70 μm and then cut into discs with a diameter of 3 mm. The discs were then polished by a twin-jet electro-polisher with an electrolyte solution consisting of 10 vol. % perchloric acid and 90 vol. % ethanol at -30 °C; a voltage of 30 V and an electric current of 20 mA were applied. Tensile tests were repeated three times at ambient temperature for each condition using an INSTRON 4468 mechanical testing system with a strain rate of 0.001 s<sup>-1</sup>; tensile tests repeated two times at 650 °C were carried out for each condition using a SHIMADZU AG-100kNE mechanical testing system with the same strain rate. The elastic modulus for each sample was determined by taking the slope of tensile curves in the elastic regime. Creep tests were repeated at least two times for each condition by a TOSHIN RT-20 creep testing machine. The chamber was heated up to 650 °C within 2 hours; 650 MPa constant stress was then applied to the specimens.

### 3. Results and analysis

#### 3.1. Microstructures

Fig. 2 presents the EBSD IPF Z maps showing the microstructure of the as-built specimens. In particular, Fig. 2 (a) and 2 (b) depict the microstructures of as-built IN718 without and with CoAl<sub>2</sub>O<sub>4</sub> taken along the transverse direction (TD), respectively; Fig. 2 (c) and 2 (d) depict the microstructures of as-built IN718 without and with CoAl<sub>2</sub>O<sub>4</sub> taken along the build direction (BD), respectively. Similar to the observations reported in previous studies [1–7], the specimens of as-built IN718 without CoAl<sub>2</sub>O<sub>4</sub> addition revealed a typical grain structure with a grid-shaped texture and elongated grains, Fig. 2 (a) and 2 (c). Interestingly, the microstructure of as-built IN718 containing CoAl<sub>2</sub>O<sub>4</sub> inoculants was distinctly different. The inoculant addition appeared to obscure the texture present in as-built microstructure (see Fig. 2 (b) and 2 (d)). This microstructural change was more evident at higher magnification, Fig. 3 (a) to (f). Fig. 3 (a), (b), and (c) show the microstructures of as-built IN718 without CoAl<sub>2</sub>O<sub>4</sub> while Fig. 3 (d), (e), and (f) show the microstructures of as-built IN718 with CoAl<sub>2</sub>O<sub>4</sub>. All as-built microstructures were comprised of a mixture of large columnar grains and fine, equiaxed grains. Microstructures of as-built IN718 without

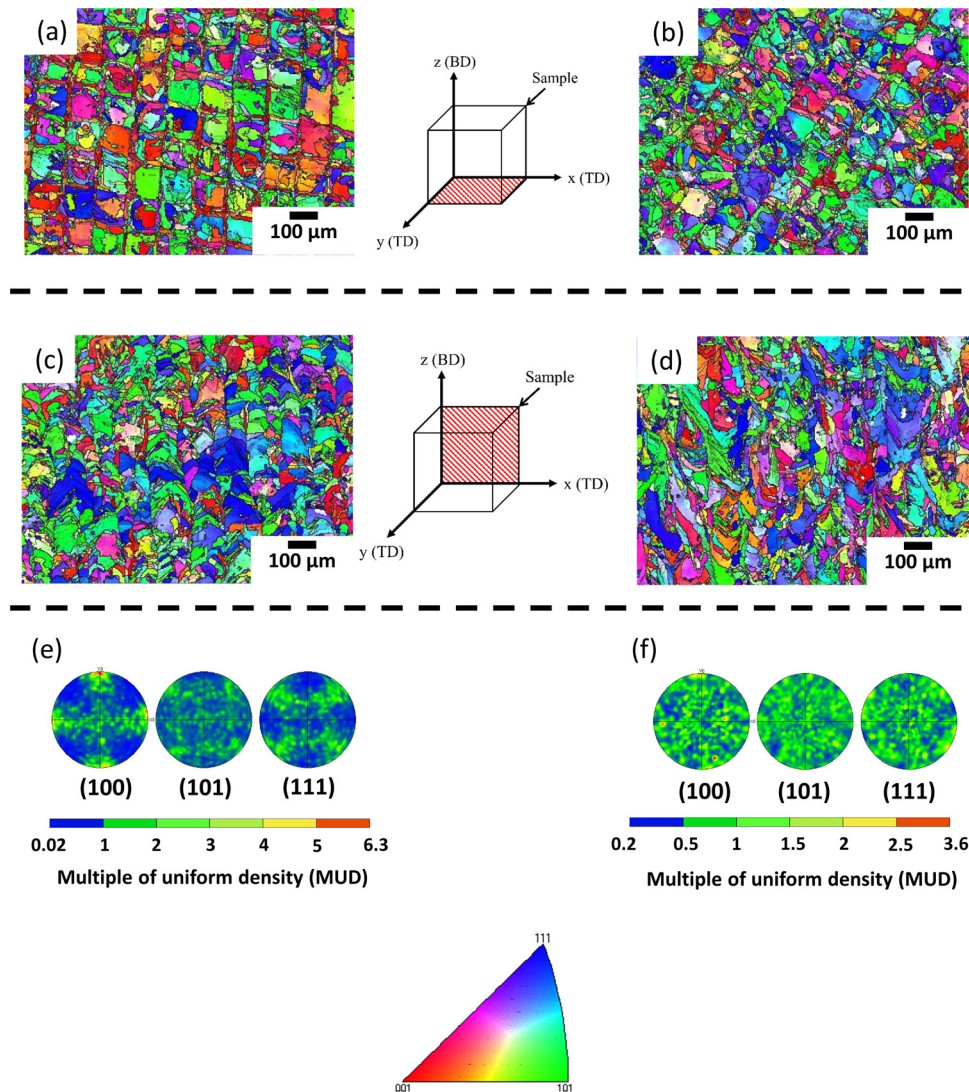
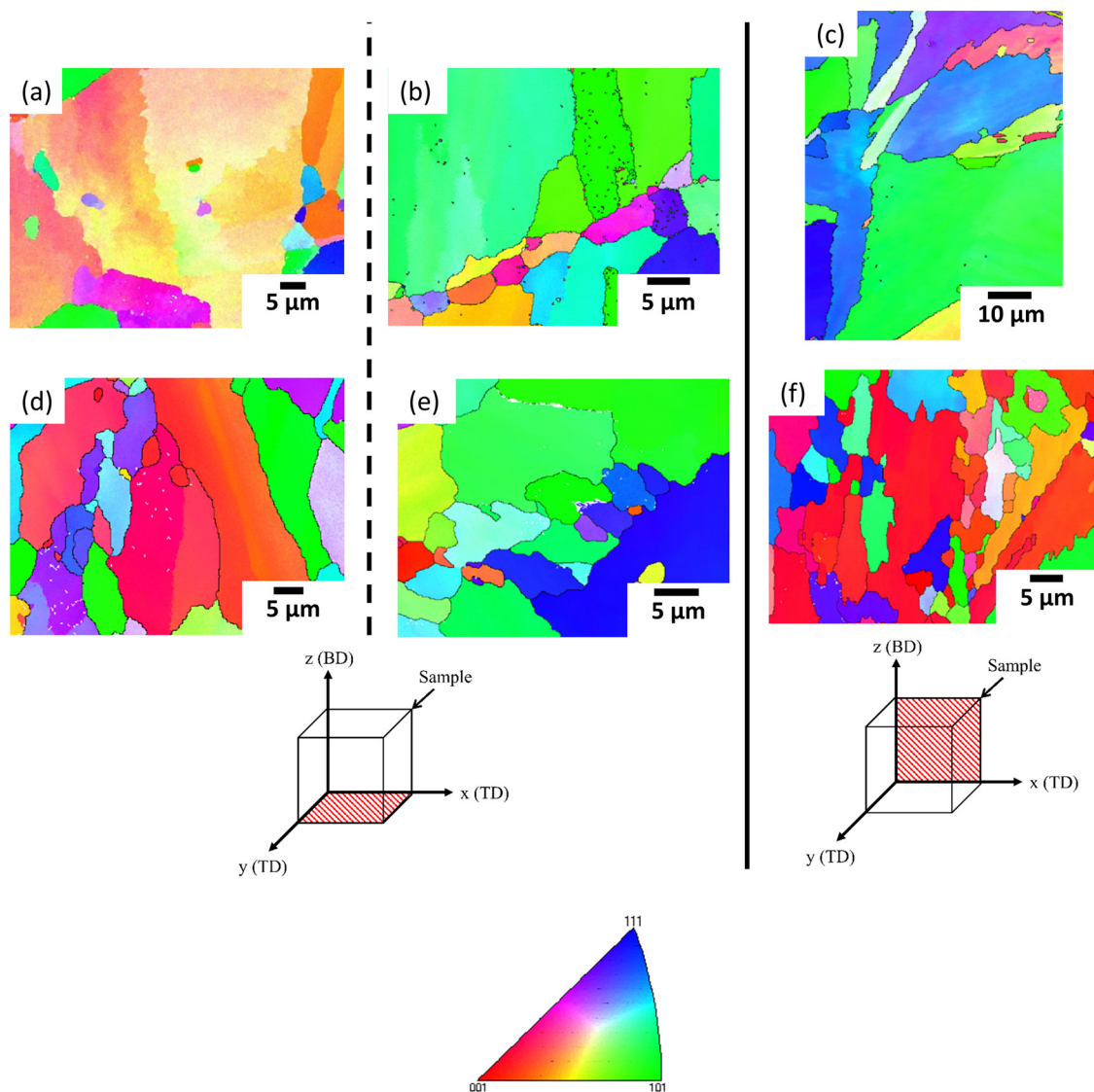


Fig. 2. EBSD Micrographs and analysis showing the microstructures of the as-built IN718. In particular, (a) and (b) depict the IPF Z maps taken along the TD (xy plane); (c) and (d) depict the IPF Z maps taken along the BD (z axis); (e) and (f) depict the pole figures with respect to the TD. Note that (a), (c), and (e) display the microstructure of as-built IN718 without CoAl<sub>2</sub>O<sub>4</sub> while (b), (d), and (f) display the microstructure of as-built IN718 with CoAl<sub>2</sub>O<sub>4</sub>.



**Fig. 3.** EBSD IPF Z maps showing the distinct microstructural features present in as-built IN718. (a), (b), and (c) display the microstructures of as-built IN718 without  $\text{CoAl}_2\text{O}_4$  while (d), (e), and (f) display the microstructures of as-built IN718 with  $\text{CoAl}_2\text{O}_4$ . Note that (a) and (d) were taken from the region generally featuring the coarse-grained region with respect to the TD (xy plane); (b), (e) and (f) were taken from the region generally featuring the fine-grained region with respect to the TD; (c) and (f) present the columnar grain structure along the BD (z axis).

inoculant contained a higher overall proportion of columnar grains and appeared to possess a higher degree of crystallographic texture. With  $\text{CoAl}_2\text{O}_4$ , on the other hand, a higher proportion of equiaxed grains were present in the microstructure. This change in the as-built microstructure directly affected the orientation of grains. According to the pole figures, Fig. 2 (e) and 2 (f), the inherent [001] and [101] texture present in as-built specimens became more diffuse with the addition of  $\text{CoAl}_2\text{O}_4$ , moreover, the local grain size distributions analysis shown in Fig. 4 indicates the reduced texture and grain refinement. Based on the line scan along the horizontal direction, Fig. 4 (a) and (b), the repeated fluctuation of grain size was less pronounced, and the grain size was generally smaller in specimens containing  $\text{CoAl}_2\text{O}_4$  particles. The average grain size distribution, Fig. 4 (c), also confirms the presence of a higher fraction of small grains which resulted in an increased area fraction of grains smaller than  $20\ \mu\text{m}$  by 3.1 % and a decreased average grain size by 15 % approximately.

Interestingly, the  $\text{CoAl}_2\text{O}_4$  inoculants seemed to influence the magnitude of residual strains in the as-built microstructure. Based on the EBSD kernel average misorientation (KAM) maps, Fig. 5 (a) and (b), the magnitude of the misorientation present in as-built IN718 with

$\text{CoAl}_2\text{O}_4$  was modestly larger and indicated that a higher amount of residual strains was retained during the SLM process. The increasing amount of residual strains could likely be attributed to the presence of a nano-oxide dispersion in the dendritic structure of as-built IN718 with  $\text{CoAl}_2\text{O}_4$ . The nano oxides were found to disperse uniformly with an average particle size of 54 nm and an area fraction of 0.3 % approximately, as shown in Fig. 5 (c) and 5 (d). A high density of dislocations was observed to surround each oxide particle. According to TEM-EDS measurements, Table 2, the nano-oxide particles presented within the microstructure were primarily enriched in Al with minimal Co content.

Fig. 6 (a) and (b) display the EBSD IPF Z maps for IN718 without and with  $\text{CoAl}_2\text{O}_4$  after the solution heat-treatment (SHT) for 2 hours at  $1100\ ^\circ\text{C}$ ; the average grain size distributions are summarized in Fig. 6 (c). Since recrystallization and grain growth occurred during this process, it could be expected that the cross-section parallel to the BD exhibited a similar grain structure to that parallel to the TD. According to Fig. 6, the microstructure of specimens without  $\text{CoAl}_2\text{O}_4$  was comprised of relatively coarse grains with an average grain size of  $32\ \mu\text{m}$  whereas the microstructure of specimens containing  $\text{CoAl}_2\text{O}_4$  particles consisted of a bimodal grain structure with an average grain size of  $21\ \mu\text{m}$ . As

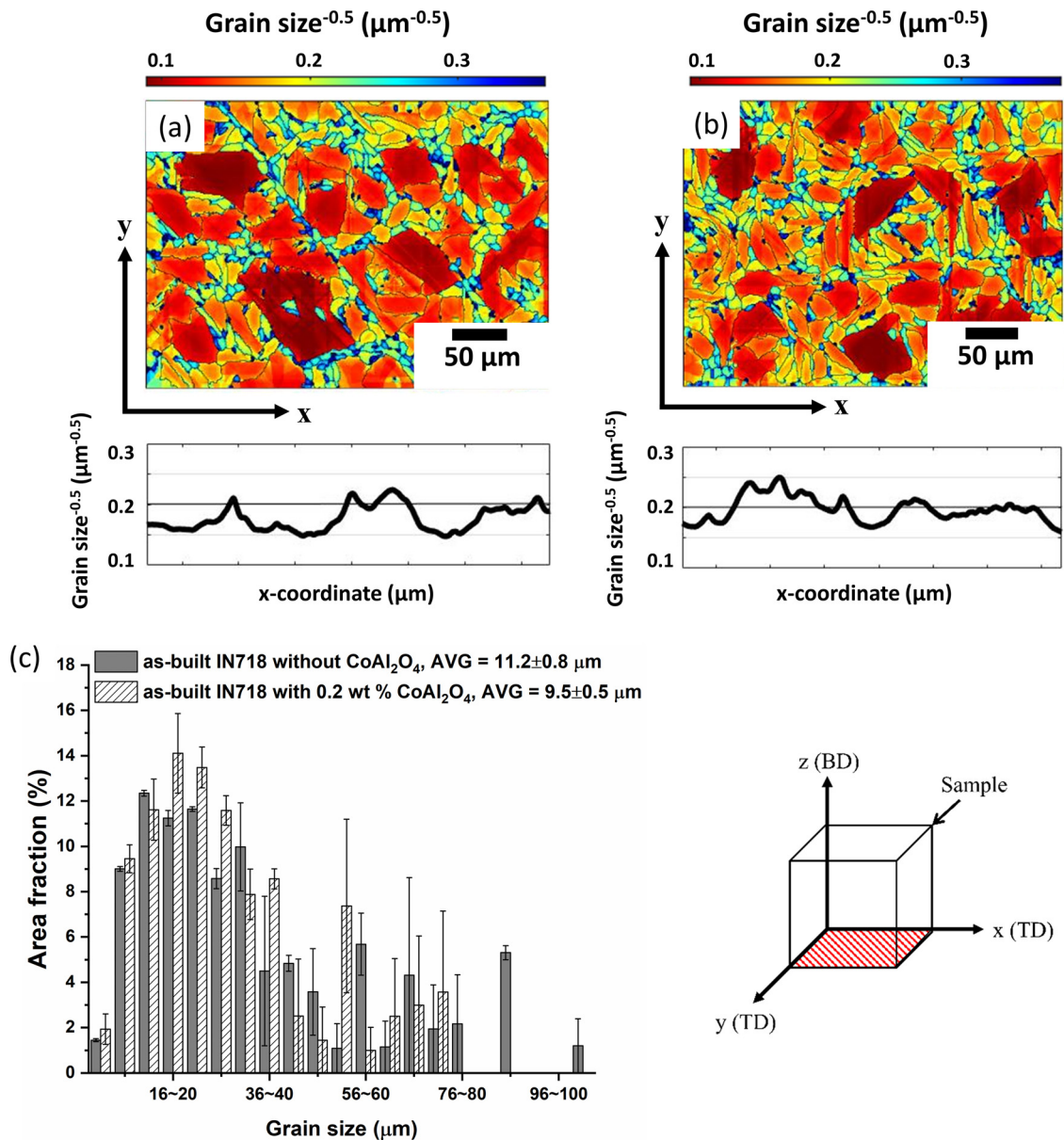


**Fig. 4.** Grain size measurements for as-built IN718 without (a) and with (b)  $\text{CoAl}_2\text{O}_4$  with respect to the TD (xy plane). The average grain size distributions of specimens with and without  $\text{CoAl}_2\text{O}_4$  were summarized in (c) where AVG indicates the average grain size. Note that the line scans presented in (a) and (b) indicate the moving average along the horizontal (x) direction. Each average was taken along the vertical (y) direction. The average grain size distributions were taken from two separated regions with the same area.

shown in Fig. 6 (d) and Table 3, the Al-rich nano oxides observed in the as-built microstructure remained unchanged following the SHT and age. In addition to nano oxides,  $\gamma'$  and  $\gamma''$  precipitates were observed. Fig. 7 shows the TEM observations of precipitates in samples with and without  $\text{CoAl}_2\text{O}_4$  after the SHT and age. As displayed in Fig. 7, both conditions possessed  $\gamma'$ - $\gamma''$  precipitates with similar size and fraction.

### 3.2. Mechanical properties

Fig. 8 (a) shows the stress-strain curves of as-built specimens at ambient temperature with the plot highlighting the elastic regime. The corresponding yield strength ( $\sigma_y$ ), ultimate tensile strength ( $\sigma_{\text{UTS}}$ ), elongation to failure (EL), and Young's modulus (E) are summarized in Table 4. Similar to the observations reported in previous works [29], the specimens of as-built IN718 were anisotropic as the measured E along the transverse direction (TD) was 1.4 times larger than that along the build direction (BD). In this study, the measured E along the TD and

BD for the specimens containing  $\text{CoAl}_2\text{O}_4$  inoculants were 217 GPa and 232 GPa, respectively. These measured values corresponded to the notable lack of crystallographic texture present in the as-built microstructure and approached those of conventional cast and wrought IN718 [30]. Following the post-heat-treatment, the anisotropy of elastic properties present in as-built specimens would be further minimized as a more homogeneous grain structure was achieved, Fig. 6 (a) and (b).

The inoculant addition also contributed to a slight increase in tensile strength. According to Table 4, the addition of  $\text{CoAl}_2\text{O}_4$  slightly increased the  $\sigma_y$  of as-built samples with respect to the TD and BD by 23 MPa and 12 MPa, respectively. The EL was measured to be greater than 30 % for all as-built specimens, so inoculants did not affect much on EL. The beneficial effect of the  $\text{CoAl}_2\text{O}_4$  inoculants on tensile properties became more pronounced following the SHT and age. Fig. 8 (b) displays the stress-strain curves of the solution and aged specimens along the TD at ambient temperature (RT) and 650 °C. The  $\sigma_y$ ,  $\sigma_{\text{UTS}}$ , EL, and E are summarized in Table 5. At ambient temperature, the  $\sigma_y$  and  $\sigma_{\text{UTS}}$  of

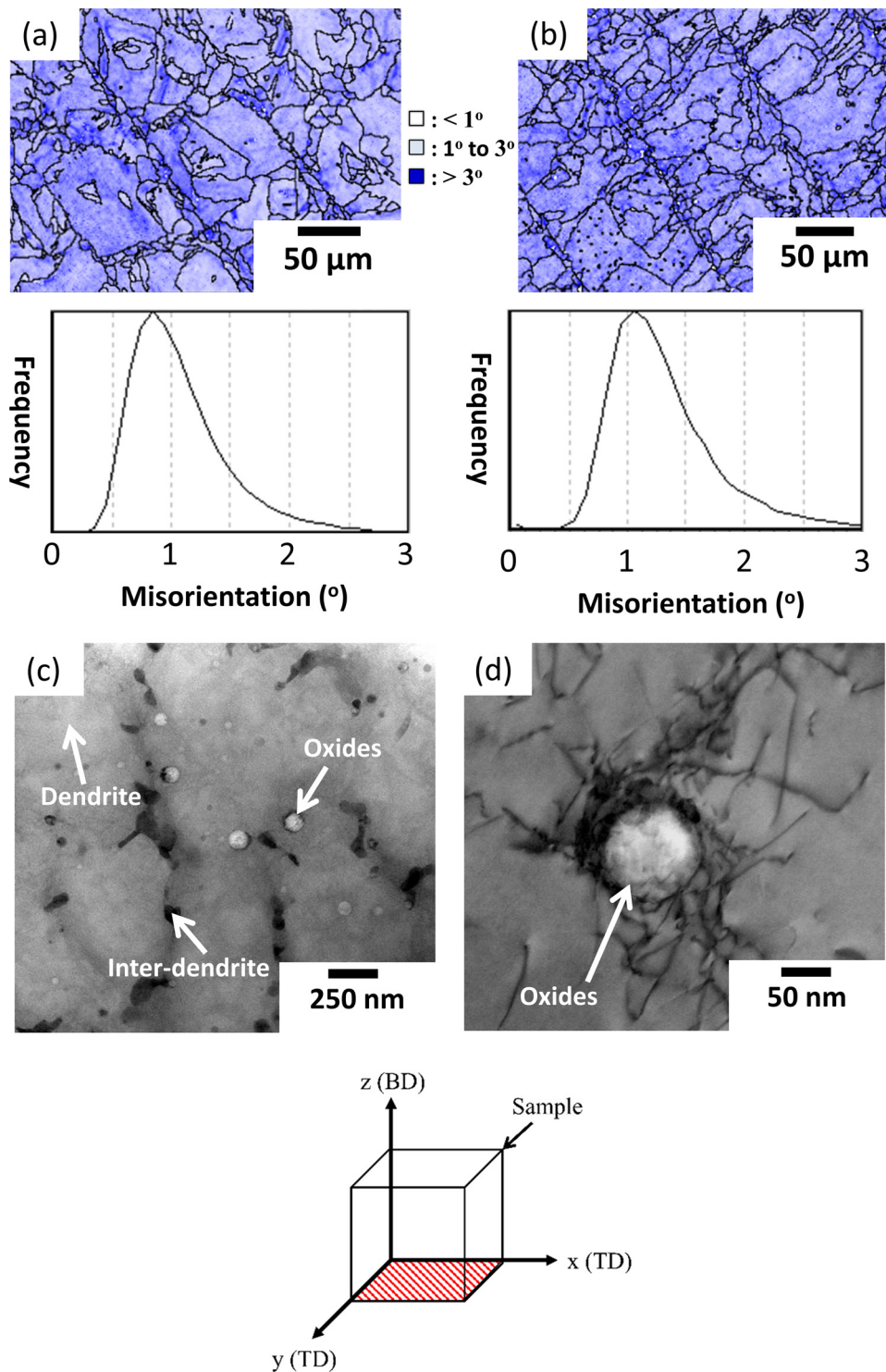


**Fig. 5.** EBSD misorientation distribution maps with misorientation profiles for the as-built IN718 without (a) and with (b)  $\text{CoAl}_2\text{O}_4$  addition with respect to the TD (xy plane). (c) and (d) display the STEM images of the as-built IN718 containing  $\text{CoAl}_2\text{O}_4$  inoculants. In particular, (c) depicts the dendritic structure with nano-oxide particles present in the matrix while (d) displays the morphology of nano-oxide particles.

**Table 2**  
Chemical composition of the various microstructural features shown in Fig. 5 (c) measured by TEM EDS.

at %	Ni	Fe	Cr	Al	Co	Ti	Mo	Nb	O
Oxides	1	0.4	0.6	32.7	0.1	1.3	0	1.8	62.1
Dendrite	51.8	19.2	21.7	0.8	0.4	1	1.9	2.9	0.3
Inter-dendrite	47.3	15.4	19.2	0.7	0	1.6	2.9	12.9	0

specimens containing  $\text{CoAl}_2\text{O}_4$  inoculants were increased by 63 MPa and 34 MPa, respectively, in average when compared to those of specimens without  $\text{CoAl}_2\text{O}_4$ . The EL was measured to be more than 20 %. Similarly, at 650 °C, the  $\sigma_y$  and  $\sigma_{UTS}$  of specimens with  $\text{CoAl}_2\text{O}_4$  addition were 66 MPa and 49 MPa higher, respectively, than those of specimens without  $\text{CoAl}_2\text{O}_4$ . The EL was measured to be 19.3 % and 16.4 % for SLM IN718 without and with  $\text{CoAl}_2\text{O}_4$ , respectively. Both the mechanical properties at ambient temperature and 650 °C were

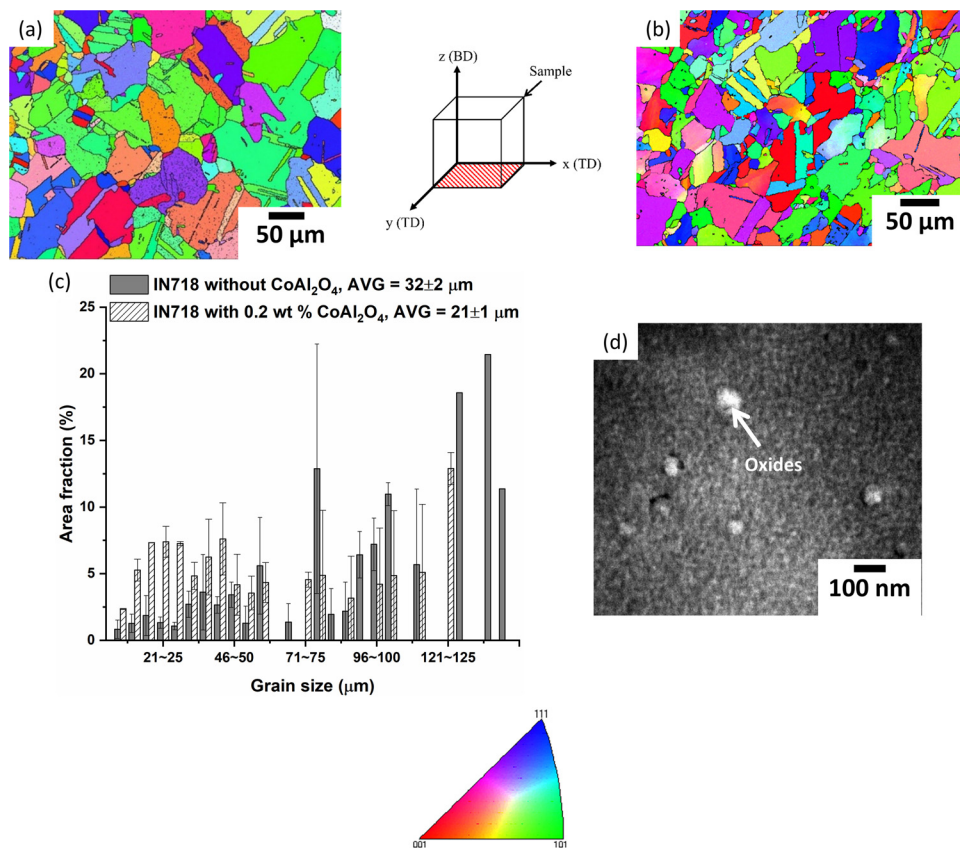


**Fig. 6.** EBSD IPF Z maps for specimens without (a) and with (b)  $\text{CoAl}_2\text{O}_4$  addition taken along the TD (xy plane) after the SHT. The average grain size distributions were summarized in (c) where AVG indicates the average grain size. STEM image (d) depicts the morphology of solution and aged IN718 with  $\text{CoAl}_2\text{O}_4$  inoculants showing a fine dispersion of nano-oxide particles in the matrix. Note that the average grain size distributions were taken from two separated regions with the same area.

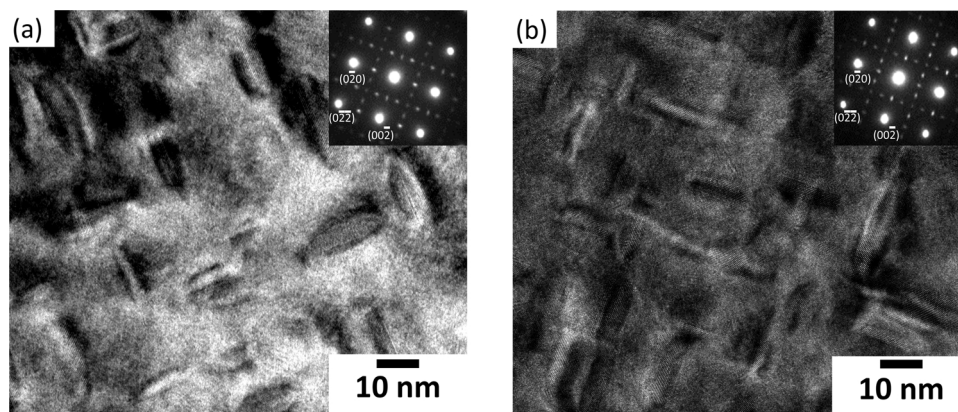
**Table 3**  
Chemical composition of the various microstructural features shown in Fig. 6 (d) measured by TEM EDS.

at %	Ni	Fe	Cr	Al	Co	Ti	Mo	Nb	O
Oxides	5.7	1.5	1.9	30.7	0.1	3.2	0.2	2.1	54.6
Matrix	50.2	18.7	21.7	0.8	0.1	1.1	2.2	3.3	1.9

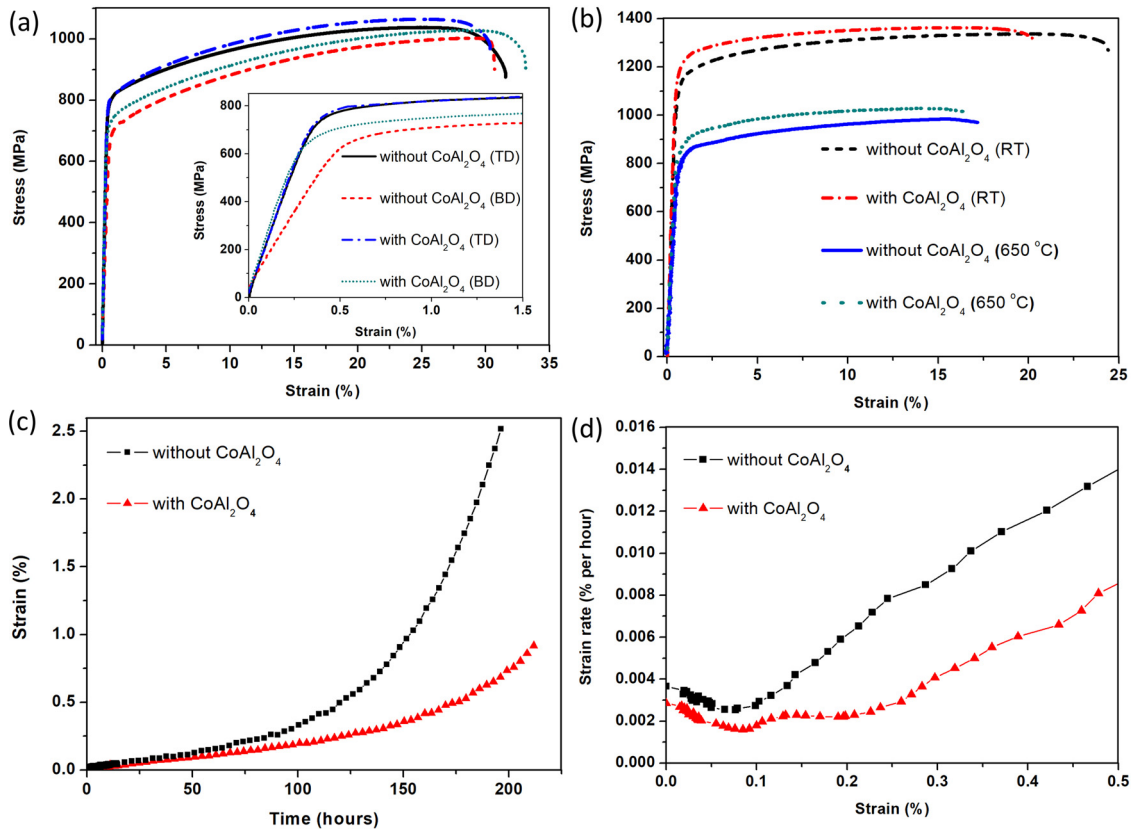
comparable to those of cast and wrought processed IN718 [30]. Interestingly, tensile testing for both SLM processed IN718 with and without  $\text{CoAl}_2\text{O}_4$  revealed a comparatively lower EL than that of cast and wrought processed IN718 at 650 °C. This decrease in EL at elevated temperature was reported in previous studies on IN718 processed by SLM and electron beam melting as well [31,32].

Fig. 8 (c) presents the creep curves of the solution and aged

specimens along the TD under 650 °C/650 MPa; the correlations between creep strain and creep strain rate are plotted in Fig. 8 (d). The corresponding average steady-state creep strain rates and rupture lives are summarized in Table 6. Both specimens showed similar curves in the primary stage and exhibited the same trend to those of wrought samples [33]. Interestingly, throughout the entire duration of the creep test, the specimens containing  $\text{CoAl}_2\text{O}_4$  exhibited a noticeable decrease in creep strain rate when compared to the samples without  $\text{CoAl}_2\text{O}_4$ , Fig. 8 (d). A comparison shows that the creep strain rate of specimens containing  $\text{CoAl}_2\text{O}_4$  is approximately  $3.9 \times 10^{-9} \text{ s}^{-1}$  lower than that of specimens without  $\text{CoAl}_2\text{O}_4$ . In addition, the strain rate started to increase steadily at a creep strain of 0.22 % for samples containing  $\text{CoAl}_2\text{O}_4$  while 0.11 % for those without  $\text{CoAl}_2\text{O}_4$ . The increasing threshold of strain for the tertiary creep and lower creep strain rate were contributed by an extended period of secondary creep.



**Fig. 7.** TEM bright field images and electron diffraction patterns from the zone axis of  $[001]_\gamma$  reflecting the  $\gamma$  phase and  $\gamma'/\gamma''$  co-precipitates in specimens without (a) and with (b)  $\text{CoAl}_2\text{O}_4$  inoculants after the SHT and age.



**Fig. 8.** Curves showing miscellaneous mechanical properties of IN718 without and with CoAl<sub>2</sub>O<sub>4</sub>. In particular, (a) displays the engineering stress-strain curves for the as-built specimens along the TD and BD at ambient temperature; the inset in (a) highlights the elastic regime of stress-strain curves; (b) depicts the engineering stress-strain curves for the solution and aged specimens along the TD at ambient temperature (RT) and 650 °C, respectively; (c) displays the creep curves for solution and aged specimens along the TD at 650 °C/650 MPa. Note that the correlations between the creep strain and creep strain rate before the beginning stage of tertiary creep are plotted in (d).

**Table 4**

Summary showing the yield strength ( $\sigma_y$ ), ultimate tensile strength ( $\sigma_{UTS}$ ), elongation to failure (EL), and elastic modulus (E) presented in Fig. 8 (a).

	$\sigma_y$ (MPa)	$\sigma_{UTS}$ (MPa)	EL (%)	E (GPa)
SLM IN718 (TD)	777 ± 10	1036 ± 11	31.4 ± 0.2	200 ± 14
SLM IN718 (BD)	700 ± 11	998 ± 20	30.8 ± 0.1	143 ± 9
SLM IN718 + CoAl <sub>2</sub> O <sub>4</sub> (TD)	800 ± 3	1069 ± 4	30.3 ± 0.1	217 ± 1
SLM IN718 + CoAl <sub>2</sub> O <sub>4</sub> (BD)	712 ± 12	1015 ± 13	32.5 ± 0.7	232 ± 7.5
SLM IN718 (TD) [29]	757, 766	1050, 1067	29, 24	222
SLM IN718 (BD) [29]	633, 583	931, 934	37, 28	165
C&W IN718 [30]	1186	1400	18.5	206

**Table 5**

Summary showing the yield strength ( $\sigma_y$ ), ultimate tensile strength ( $\sigma_{UTS}$ ), elongation to failure (EL), and elastic modulus (E) presented in Fig. 8 (b).

	$\sigma_y$ (MPa)	$\sigma_{UTS}$ (MPa)	EL (%)	E (GPa)
<b>RT</b>				
SLM IN718	1098 ± 5	1329 ± 7	24 ± 0.3	200 ± 7
SLM IN718 + CoAl <sub>2</sub> O <sub>4</sub>	1161 ± 6	1363 ± 2	20.2 ± 0.2	208 ± 3
C&W IN718 [30]	1186	1400	18.5	208
<b>650 °C</b>				
SLM IN718	800 ± 2	987 ± 2	19.3 ± 2.2	134 ± 5
SLM IN718 + CoAl <sub>2</sub> O <sub>4</sub>	866 ± 4	1036 ± 6	16.7 ± 0.3	145 ± 2
C&W IN718 [30]	1000	1124	26	172

Consequently, the rupture life was prolonged from 177 hours to 229 hours. It should be noted that, however, the maximum creep strain decreased from 2.45 % to 1.64 % in sample containing CoAl<sub>2</sub>O<sub>4</sub>, implying that the addition of CoAl<sub>2</sub>O<sub>4</sub> might have led to a slight decrease

**Table 6**

Summary showing the average of creep properties presented in Fig. 8 (c) and 8 (d).

	Steady strain rate (10 <sup>-9</sup> s <sup>-1</sup> )	Rupture life (h)
SLM IN718	8.8 ± 2.6	177 ± 21
SLM IN718 + CoAl <sub>2</sub> O <sub>4</sub>	4.9 ± 0.3	229 ± 17

in ductility. Microstructural characterization of crept samples was performed and displayed in Fig. 9 (a) to (f). In Fig. 9 (d) and (e), Al-rich nano-oxides were observed in samples containing CoAl<sub>2</sub>O<sub>4</sub>, and they appeared to pin dislocations and grain boundaries when compared to the straight slip band and grain boundaries present in specimens without CoAl<sub>2</sub>O<sub>4</sub>, Fig. 9 (a) and (b). In addition, the EBSD analysis shown in Fig. 9 (c) and (f), reveal that intergranular cracks dominated the fractures in crept samples.

**4. Discussion**

**4.1. Formation of grain structure**

CoAl<sub>2</sub>O<sub>4</sub> inoculants have been known to facilitate grain nucleation by the formation of Co and CoAl particles during solidification of superalloys cast [22–24], and the present study has focused on understanding how CoAl<sub>2</sub>O<sub>4</sub> inoculants could impact the crystallographic texture, grain size, and mechanical properties of IN718 processed by SLM. It is known that the solidification structure is closely associated with the thermal gradients (G denoted in the units of K/m) and the solidification rate (V denoted in the units of m/s). According to the

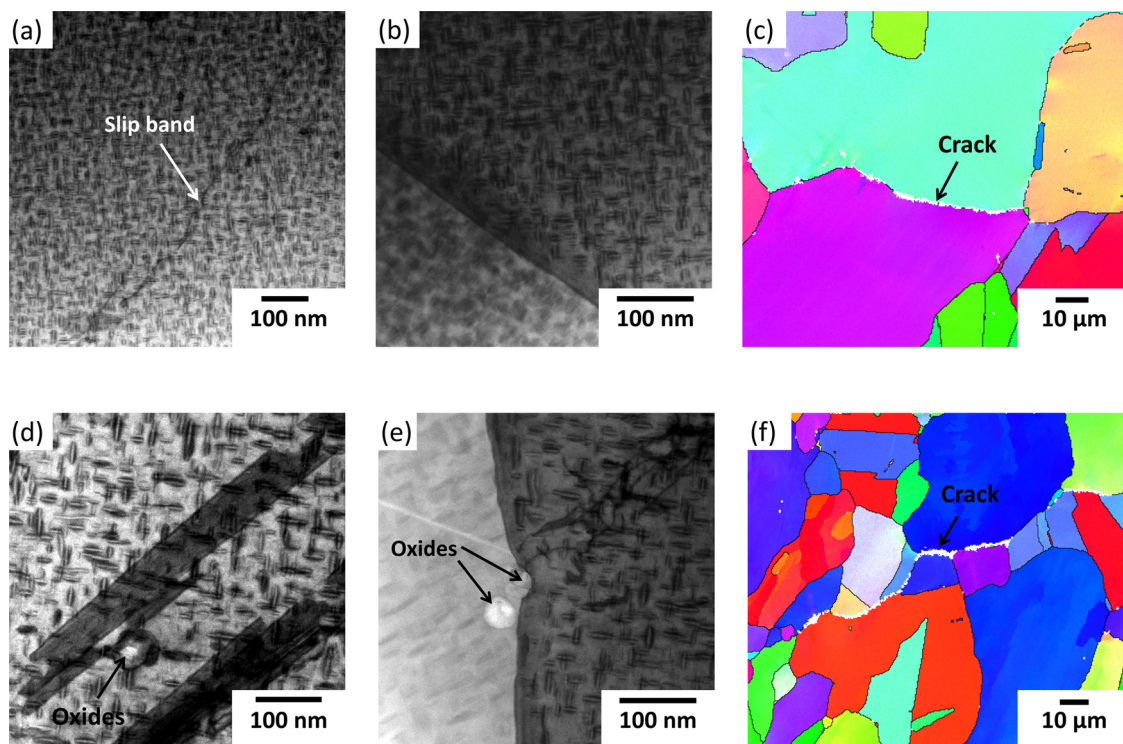


**Fig. 9.** Morphology showing distinct features present in the cross-section of crept samples. In particular, (a), (b), and (c) display the microstructures of IN718 specimens without  $\text{CoAl}_2\text{O}_4$  while (d), (e), and (f) display the microstructures of IN718 with  $\text{CoAl}_2\text{O}_4$ . (a) and (d) are the STEM bright field images showing slip bands within the grain; (b) and (e) are the STEM bright field images showing the morphology of grain boundary; (c) and (f) are the EBSD IPF Z maps showing the intergranular cracks.

criterion proposed in a previous work [34], the microstructure will be predominately columnar when:

$$\frac{G^n}{V} > a \left( 8.6 \Delta T_0 \frac{N_0^{1/3}}{n+1} \right)^n \quad (1)$$

Here,  $\Delta T_0$  is the equilibrium liquidus-solidus interval,  $N_0$  is the nucleation density,  $a$  and  $n$  are the alloy constants. It could be seen that an increase in  $G$  and decrease in  $V$  favors the growth of columnar grains, whereas increasing  $V$  and decreasing  $G$  favors the growth of more equiaxed grains. This trend is also consistent with several models used for predicting the solidification behaviors of other alloys [35–37].

During the SLM process, the zig-zag scanning strategy with a single energy spot was moving back and forth rapidly, and hence the melt pool induced could be considered as a “band” with a width corresponding to the hatch distance of 100  $\mu\text{m}$ . In the middle of the band, the steep thermal gradient perpendicular to the melt pool boundary and the comparatively lower solidification rate induced the formation of coarse, columnar grains [38], Fig. 3 (a) and (c). These grains would have a preferential [001] direction aligned closely with the thermal gradient, which was close to the BD. The orientation preference imparted an elongated grained structure with a high degree of anisotropy in as-built IN718 (see Fig. 2 (c) and (e)). At either end of the band, the surrounding solid materials would dissipate the thermal energy from the laser. The lower thermal gradient and more rapid solidification rate promoted the formation of fine grains with random orientations, Fig. 3 (b); the rotation of scanning pattern by 67° between successive layers resulted in the grid-shaped texture with respect to the TD, Fig. 2 (a). With  $\text{CoAl}_2\text{O}_4$ , there was a fine dispersion of nano-oxide particles throughout the microstructure, and these oxides appeared to facilitate the formation of fine equiaxed grains in the middle of the band, Fig. 3 (d), and (f). Consequently, a finer grain structure with less crystallographic texture could be achieved to reduce the degree of elastic anisotropy.

The fine dispersion of Al-rich nano-oxide particles is likely the result

of the chemical reduction of  $\text{CoAl}_2\text{O}_4$  within the melt pool of IN718 during processing. Investigations pertaining to the effect of  $\text{CoAl}_2\text{O}_4$  inoculants on investment cast Ni-base superalloys [22–24] reported that  $\text{CoAl}_2\text{O}_4$  could decompose into various oxides, including  $\text{Al}_2\text{O}_3$ ,  $\text{TiO}_2$ , and  $\text{Cr}_2\text{O}_3$ , during solidification. This is consistent with the findings of present study as all of the oxide particles were found to be absent of Co and enriched with either Al or Ti (see Table 3). Furthermore, the free enthalpy of chemical reactions between  $\text{CoAl}_2\text{O}_4$  and Al, Ti, and Cr are -250 kJ, -180 kJ, and -100 kJ, respectively, at 1300 °C [23]. Thereby, the driving force for the formation of  $\text{Al}_2\text{O}_3$  should be higher than those of other oxides, which is also consistent with the high Al content measured in the oxide particles. The presence of the oxide dispersion was expected to exert a Zener pinning pressure to grain boundaries [25], preventing grain coarsening during the repeated heating induced by SLM process; this effect also assisted to maintain a finer grain structure in IN718 with  $\text{CoAl}_2\text{O}_4$  after the post-heat-treatment.

#### 4.2. Mechanical properties

The improvement of mechanical properties in SLM processed IN718 with  $\text{CoAl}_2\text{O}_4$  can be directly attributed to the microstructure evolution. In order to better understand the underlying mechanism of how the addition of the  $\text{CoAl}_2\text{O}_4$  inoculant addition could affect mechanical properties, various factors are considered. The contribution of precipitation strengthening is determined by the size, morphology, volume fraction, and composition of precipitates. Following the SHT and age, the microstructure of both IN718 with and without  $\text{CoAl}_2\text{O}_4$  were found to be nominally identical and consist of  $\gamma'$ - $\gamma''$  precipitates with similar morphologies, size, and fraction. Moreover, the overall chemical composition was similar to that of IN718 powder before printing. Therefore, the decomposition of  $\text{CoAl}_2\text{O}_4$  does not significantly impact the bulk or local chemistry. In other words, the degree of precipitation strengthening from  $\gamma'$  and  $\gamma''$  precipitates does not appear to be affected by the

addition of  $\text{CoAl}_2\text{O}_4$  inoculants in present study.

The contribution of grain size to  $\sigma_y$  is ascribed to the fraction of grain boundaries that can impede dislocation movements. This relationship can be described by the Hall-Petch relation:

$$(\sigma_y)_{\text{Hall-Petch}} = \sigma_{y0} + k/\sqrt{d} \quad (2)$$

where  $\sigma_{y0}$  is the intrinsic flow stress constant,  $k$  is the strengthening coefficient,  $d$  is the average grain size. Based on the Hall-Petch strengthening parameters reported for IN718 [39], the decrease of the average grain size from 32  $\mu\text{m}$  to 21  $\mu\text{m}$  could only increase the strength by 10 MPa approximately. Thus, the changes in the grain size alone cannot explain the differences in increasing strength measured in specimens with  $\text{CoAl}_2\text{O}_4$ . This analysis suggests that the nano-oxide particles may also contribute to the increase in tensile strength. Generally, oxide dispersion strengthening (ODS) is associated with a repulsive interaction between dislocations and nano-oxide particles as an additional bowing stress is required for dislocations to bypass the nano-oxide particles [40]. The noticeable increases in  $\sigma_y$  by 63 MPa and 66 MPa at ambient temperature and 650 °C, respectively, for samples with inoculants would be consistent with the contribution from ODS.

The general deformation mechanism for the creep of IN718 could be evaluated by using the creep deformation mechanism map [41]. Incorporating the liquidus temperature of 1260 °C and Young's modulus of 208 GPa [30], it could be deduced that dislocation glide was likely the rate-controlling step for creep of IN718 at 650 °C and 650 MPa. The dispersion of Al-rich nano-oxide particles was expected to exert a counteractive force to dislocations and restrict their mobility, Fig. 9 (d). Simultaneously, additional stresses would be required to separate dislocations from the particle-matrix interface as the interfaces between the Al-rich oxides and FCC matrix are not coherent [42]. Each of these mechanisms described would contribute to increasing the magnitude of the threshold stress required to activate the dislocation movement, leading to a decrease in creep strain rate.

The present study has demonstrated that  $\text{CoAl}_2\text{O}_4$  inoculants lead to the formation of a fine dispersion of oxide particles in the microstructure after SLM of IN718. Chemical reduction of the  $\text{CoAl}_2\text{O}_4$  particles within the melt pool during SLM could promote nucleation of equiaxed grains with random orientations during solidification. This contributed to reducing the degree of crystallographic anisotropy that is characteristic of fusion based additive manufacturing processes. Moreover, the Zener pinning force induced by the presence of oxide particles also appeared to maintain a fine grain structure following a post-heat-treatment. The fine dispersion of nano-oxide particles combined with the refined grain structure contributed to an increase in  $\sigma_y$  at room temperature and 650 °C, as well as a modest decrease in creep strain rate and increased creep rupture life. Results from this study clearly show that minor additions of inoculants could optimize the microstructures and improve mechanical properties of SLM processed materials.

## 5. Conclusions

During the SLM process,  $\text{CoAl}_2\text{O}_4$  inoculants were found to chemically react with the IN718 melt pool, resulting in a dispersion of Al-rich nano-oxide particles. The inoculant addition also triggered the formation of equiaxed grains with random orientations and reduced the degree of crystallographic texture present in the as-built microstructure. Furthermore, the Zener pinning force yielded by these nano-oxide particles appeared to hinder the grain growth during the post-heat-treatment, leading to a refined grain structure. Tensile testing revealed that the SLM processed IN718 with  $\text{CoAl}_2\text{O}_4$  inoculants exhibited a more isotropic elastic moduli along both the TD and BD. Following the SHT and age, the tensile yield strength of SLM processed IN718 with  $\text{CoAl}_2\text{O}_4$  inoculants were increased by 63 MPa and 66 MPa at room temperature and 650 °C, respectively. Creep testing revealed that the

steady creep strain rate was decreased from  $8.8 \times 10^{-9} \text{ s}^{-1}$  to  $4.9 \times 10^{-9} \text{ s}^{-1}$ , and creep rupture life was increased from 177 hours to 229 hours in SLM IN718 samples processed with a 0.2 wt. % addition of  $\text{CoAl}_2\text{O}_4$ .

## Declaration of Competing Interest

None.

## CRediT authorship contribution statement

**I-Ting Ho:** Conceptualization, Methodology, Investigation, Validation, Data curation, Visualization, Writing - original draft. **Tzu-Hou Hsu:** Investigation, Validation. **Yao-Jen Chang:** Investigation, Methodology, Validation. **Chen-Wei Li:** Investigation, Validation. **Kai-Chun Chang:** Investigation, Validation. **Sammy Tin:** Writing - review & editing, Supervision. **Koji Kakehi:** Resources. **An-Chou Yeh:** Writing - review & editing, Supervision.

## Acknowledgment

This work was supported by the National Science Foundation (NSF), U.S.A. [grant number CMMI # 1663068], and the Ministry of Science and Technology (MOST), Taiwan [grant numbers: MOST108-2218-E-007-009]; the authors would also like to acknowledge Mr. Dhruv Tiparti in Illinois Institute of Technology for his help during microstructural characterization.

## References

- [1] F. Brenne, A. Taube, M. Pröbstle, S. Neumeier, D. Schwarze, M. Schaper, T. Niendorf, Microstructural design of Ni-base alloys for high-temperature applications: impact of heat treatment on microstructure and mechanical properties after selective laser melting, *Progress in Additive Manufacturing* 1 (3-4) (2016) 141–151.
- [2] J. Strößner, M. Terock, U. Glatzel, Mechanical and Microstructural Investigation of Nickel-Based Superalloy IN718 Manufactured by Selective Laser Melting (SLM), *Advanced Engineering Materials* 17 (8) (2015) 1099–1105.
- [3] M. Pröbstle, S. Neumeier, J. Hopfenmüller, L. Freund, T. Niendorf, D. Schwarze, M. Göken, Superior creep strength of a nickel-based superalloy produced by selective laser melting, *Materials Science and Engineering: A* 674 (2016) 299–307.
- [4] K. Amato, S. Gaytan, L. Murr, E. Martinez, P. Shindo, J. Hernandez, S. Collins, F. Medina, Microstructures and mechanical behavior of Inconel 718 fabricated by selective laser melting, *Acta Materialia* 60 (5) (2012) 2229–2239.
- [5] D. Deng, R.L. Peng, H. Brodin, J. Moverare, Microstructure and mechanical properties of Inconel 718 produced by selective laser melting: sample orientation dependence and effects of post heat treatments, *Materials Science and Engineering: A* (2017).
- [6] M.D. Sangid, T.A. Book, D. Naragani, J. Rotella, P. Ravi, P. Kenesei, J.-S. Park, H. Sharma, J. Almer, X. Xiao, Role of heat treatment and build orientation in the microstructure sensitive deformation characteristics of IN718 produced via SLM additive manufacturing, *Additive Manufacturing* 22 (2018) 479–496.
- [7] W.M. Tucho, P. Cuvillier, A. Sjolyst-Kverneland, V. Hansen, Microstructure and hardness studies of Inconel 718 manufactured by selective laser melting before and after solution heat treatment, *Materials Science and Engineering: A* 689 (2017) 220–232.
- [8] M. Ni, C. Chen, X. Wang, P. Wang, R. Li, X. Zhang, K. Zhou, Anisotropic tensile behavior of in situ precipitation strengthened Inconel 718 fabricated by additive manufacturing, *Materials Science and Engineering: A* 701 (2017) 344–351.
- [9] Y.-L. Kuo, S. Horikawa, K. Kakehi, Effects of build direction and heat treatment on creep properties of Ni-base superalloy built up by additive manufacturing, *Scripta Materialia* 129 (2017) 74–78.
- [10] W. Huang, J. Yang, H. Yang, G. Jing, Z. Wang, X. Zeng, Heat treatment of Inconel 718 produced by selective laser melting: Microstructure and mechanical properties, *Materials Science and Engineering: A* 750 (2019) 98–107.
- [11] D. Zhang, Z. Feng, C. Wang, W. Wang, Z. Liu, W. Niu, Comparison of microstructures and mechanical properties of Inconel 718 alloy processed by selective laser melting and casting, *Materials Science and Engineering: A* 724 (2018) 357–367.
- [12] X. Li, J. Shi, C. Wang, G. Cao, A. Russell, Z. Zhou, C. Li, G. Chen, Effect of heat treatment on microstructure evolution of Inconel 718 alloy fabricated by selective laser melting, *Journal of Alloys and Compounds* 764 (2018) 639–649.
- [13] J.H. Martin, B.D. Yahata, J.M. Hundley, J.A. Mayer, T.A. Schaedler, T.M. Pollock, 3D printing of high-strength aluminium alloys, *Nature* 549 (7672) (2017) 365–369.
- [14] V. Villaret, F. Deschaux-Beaume, C. Bordreuil, A solidification model for the columnar to equiaxed transition in welding of a Cr-Mo ferritic stainless steel with Ti as inoculant, *Journal of Materials Processing Technology* 233 (2016) 115–124.

- [15] M. Bermingham, D. StJohn, J. Krynen, S. Tedman-Jones, M. Dargusch, Promoting the columnar to equiaxed transition and grain refinement of titanium alloys during additive manufacturing, *Acta Materialia* 168 (2019) 261–274.
- [16] B. AlMangour, D. Grzesiak, J.-M. Yang, Scanning strategies for texture and anisotropy tailoring during selective laser melting of TiC/316L stainless steel nanocomposites, *Journal of Alloys and Compounds* 728 (2017) 424–435.
- [17] B. Li, B. Qian, Y. Xu, Z. Liu, J. Zhang, F. Xuan, Additive manufacturing of ultrafine-grained austenitic stainless steel matrix composite via vanadium carbide reinforcement addition and selective laser melting: Formation mechanism and strengthening effect, *Materials Science and Engineering: A* 745 (2019) 495–508.
- [18] L. Xi, P. Wang, K. Prashanth, H. Li, H. Prykhodko, S. Scudino, I. Kaban, Effect of TiB<sub>2</sub> particles on microstructure and crystallographic texture of Al-12Si fabricated by selective laser melting, *Journal of Alloys and Compounds* 786 (2019) 551–556.
- [19] W.-h. Xiao, S.-q. Lu, Y.-c. Wang, S. Jing, Mechanical and tribological behaviors of graphene/Inconel 718 composites, *Transactions of Nonferrous Metals Society of China* 28 (10) (2018) 1958–1969.
- [20] D. Gu, H. Zhang, D. Dai, M. Xia, C. Hong, R. Poprawe, Laser additive manufacturing of nano-TiC reinforced Ni-based nanocomposites with tailored microstructure and performance, *Composites Part B: Engineering* 163 (2019) 585–597.
- [21] T. Rong, D. Gu, Q. Shi, S. Cao, M. Xia, Effects of tailored gradient interface on wear properties of WC/Inconel 718 composites using selective laser melting, *Surface and Coatings Technology* 307 (2016) 418–427.
- [22] H. Matysiak, M. Zagorska, A. Balkowiec, B. Adamczyk-Cieslak, K. Dobkowski, M. Koralnik, R. Cygan, J. Nawrocki, J. Cwajna, K.J. Kurzydowski, The Influence of the Melt-Pouring Temperature and Inoculant Content on the Macro and Microstructure of the IN713C Ni-Based Superalloy, *JOM* 68 (1) (2016) 185–197.
- [23] F. Binczyk, J. Sleziona, P. Gradon, Modification of the macrostructure of nickel superalloys with cobalt nanoparticles, *Composites* 1 (2011) 49–55.
- [24] F. Jian, Y. Bin, Investigation of the surface grain refinement for superalloys castings, *High Temperature Alloys for Gas Turbines* (1982) 987–997.
- [25] M. PA, M. Ferry, T. Chandra, Five decades of the Zener equation, *ISIJ international* 38 (9) (1998) 913–924.
- [26] P. Páramo-Kañetas, U. Öztürk, J. Calvo, J.M. Cabrera, M. Guerrero-Mata, High-temperature deformation of delta-processed Inconel 718, *Journal of Materials Processing Technology* 255 (2018) 204–211.
- [27] V. Beaubois, J. Huez, S. Coste, O. Brucelle, J. Lacaze, Short term precipitation kinetics of delta phase in strain free Inconel\* 718 alloy, *Materials science and technology* 20 (8) (2004) 1019–1026.
- [28] M.H.N, Edition, vol. 4 Heat Treating, ASM Heat Treating Division Council, (1981).
- [29] M. Seifi, A.A. Salem, D.P. Satko, R. Grylls, J.J. Lewandowski, Effects of Post-processing on Microstructure and Mechanical Properties of SLM-Processed IN-718, *Proceedings of the 9th International Symposium on Superalloy 718 & Derivatives: Energy, Aerospace, and Industrial Applications*, Springer, 2018, pp. 515–526.
- [30] S. metals, *High Performance Alloys Literature*, (2019) <http://www.specialmetals.com/tech-center/alloys.html>.
- [31] T. Trosch, J. Ströfner, R. Völkl, U. Glatzel, Microstructure and mechanical properties of selective laser melted Inconel 718 compared to forging and casting, *Materials letters* 164 (2016) 428–431.
- [32] M. Kirka, K. Unocic, N. Raghavan, F. Medina, R. Dehoff, S. Babu, Microstructure development in electron beam-melted Inconel 718 and associated tensile properties, *Jom* 68 (3) (2016) 1012–1020.
- [33] Z. Xu, J. Murray, C. Hyde, A. Clare, Effect of post processing on the creep performance of laser powder bed fused Inconel 718, *Additive Manufacturing* 24 (2018) 486–497.
- [34] M. Gäumann, C. Bezencon, P. Canalis, W. Kurz, Single-crystal laser deposition of superalloys: processing–microstructure maps, *Acta materialia* 49 (6) (2001) 1051–1062.
- [35] L. Nastac, J. Valencia, M. Tims, F. Dax, Advances in the Solidification of IN718 and RS5 Alloys, *Superalloys 718* (2001) 625–706.
- [36] W. Kurz, C. Bezencon, M. Gäumann, Columnar to equiaxed transition in solidification processing, *Science and technology of advanced materials* 2 (1) (2001) 185.
- [37] J. Spittle, Columnar to equiaxed grain transition in as solidified alloys, *International Materials Reviews* 51 (4) (2006) 247–269.
- [38] A.A. Antony, J. Meyer, P. Prangnell, Effect of build geometry on the  $\beta$ -grain structure and texture in additive manufacture of Ti6Al4V by selective electron beam melting, *Materials characterization* 84 (2013) 153–168.
- [39] Y.-T. Chen, A.-C. Yeh, M.-Y. Li, S.-M. Kuo, Effects of processing routes on room temperature tensile strength and elongation for Inconel 718, *Materials & Design* 119 (2017) 235–243.
- [40] U. Kocks, Statistical treatment of penetrable obstacles, *Canadian Journal of Physics* 45 (2) (1967) 737–755.
- [41] M.F. Ashby, A first report on deformation-mechanism maps, *Acta Metallurgica* 20 (7) (1972) 887–897.
- [42] E. Arzt, D. Wilkinson, Threshold stresses for dislocation climb over hard particles: the effect of an attractive interaction, *Acta Metallurgica* 34 (10) (1986) 1893–1898.